# A finite element model for impact simulation with laminated glass

M. Timmel[a], S. Kolling[b],[*], P. Osterrieder[c], P.A. Du Bois[d]

[a]University of Leipzig, Institute for Structural Mechanics, Marschnerstr. 31, 04109 Leipzig, Germany
[b]DaimlerChrysler AG, EP/SPB, HPC X271, 71059 Sindelfingen, Germany
[c]University of Cottbus, Universitätsplatz 3-4, 03044 Cottbus, Germany
[d]Freiligrathstr. 6, 63071 Offenbach, Germany

## Abstract

A computational technique for the modelling of laminated safety glass is presented using an explicit finite element solver. Coincident finite elements are used to model the layered set-up of laminated glass: shell elements with brittle failure for the glass components and membrane elements to simulate the ultimate load carrying capacity of the PVB-interlayer. Two different approaches are considered to model laminated glass: a physical model and a smeared model. In the physical model the glass is considered as elastic/brittle and the interlayer as a hyperelastic material. For the hyperelastic description of the interlayer, we give an overview of material models, which are widely used for explicit solvers, i.e. the laws by Blatz–Ko, Mooney–Rivlin and Ogden. The obtained stress–strain curves are fitted to experimental results of the interlayer. The hyperelastic model is applied to a simple impact test demonstrating the numerical robustness. In the smeared model, we use two shell elements of equal thickness with elasto-plastic material properties to obtain an improved bending response after fracture. For validation, experimental investigations have been carried out where a spherical impactor was shot against a windscreen. The acceleration of the impactor has been measured in this test and is compared to the numerical results.
© 2006 Elsevier Ltd. All rights reserved.

*Keywords:* Safety glass; Windscreen; Hyperelasticity; Explicit FEM; Short-time dynamics

## 1. Introduction

Safety glass is wide spread in industrial applications, e.g., in automotive structures. On the one hand to increase the time and effort required to gain unauthorized entry to a motor vehicle and, on the other hand, to avoid serious injuries of the passengers, e.g. after gravel impact, see [1]. In general, glass can be classified by its fracture behaviour: Conventional floatglass, which is usually applied for windows, has sharp and large splinters and cannot be used as safety glass; if floatglass is tempered, the fragments are small and blunt and it can be used as safety glass. The basic construction of laminated glass, e.g. a windscreen, involves two pieces of

*Corresponding author. Tel.: +49 7031 9082829; fax: +49 7031 9078837.
*E-mail address:* stefan.kolling@daimlerchrysler.com (S. Kolling).

floatglass together with a polyvinyl butyral (PVB) interlayer. In the case of an impact, the splinters are joined additionally by this PVB-interlayer. In short-time dynamics, the elastic behaviour for small deformations of the composite is determined by the glass. For large deformation, the PVB-interlayer plays a dominant role because the brittle glass cannot withstand large strains: The glass layers fail and the PVB-interlayer still has a load-carrying capacity left which can be observed experimentally. One situation in which this behaviour may be expected is a roof crash, following an over-roll or a cork screw flight. Thus, we have to consider two extreme cases: the glass fails or it does not fail. If the glass fails, only the interlayer (reinforced with some splinters of glass) has a load-carrying capacity left.

In the numerical simulation with the explicit solver LS-DYNA, see [6,7], the interlayer is modelled either as a hyperelastic membrane or the properties may be smeared by an elasto-plastic law. In both cases, viscous effects are neglected. The glass layers are modelled with shell elements considering maximum strain at failure as erosion criterion, i.e. failed elements are deleted from further computation. Some results of the presented model have been published in [2,3]. Numerical results obtained by an alternative model based on fracture mechanics can be found in [4], however, without applications to dynamic loading. Apart from crashworthiness analysis, verification tests and structures subjected to blast loads are further topics under considerable investigation.

## 2. Polyvinyl butyral (PVB) interlayer

### 2.1. Strain rate and temperature dependency

For many polymers, only quasistatic experimental data for different temperatures exist. In short-time dynamics, the strain rate dependency plays a dominant role. However, there is a relationship between the behaviour for different strain rates and for different temperatures. A polymer behaves qualitatively the same if we increase the strain rate or if we decrease the temperature. This finding is purely empirical and cannot be derived from a thermodynamic principle in general. The response of the PVB-interlayer varies from rubbery elastic at low strain rates to glasslike linear elastic for high strain rates. The rubber-like behaviour of the PVB can be modelled by using an hyperelastic material law.

The shear modulus of the PVB-interlayer is depicted in Fig. 1 for temperatures between −5 and +58 °C. The experimental data is taken from D'Haene [5] and shows the strong dependency of the elastic constants on the temperature. This implies a similar sensitivity due to strain rate. Especially at room temperature, there is a steep gradient in the curve (glass transition). Additionally, there is also a strong dependency on the humidity, UV-light and aging, which results in extreme conditions for experimental work. Furthermore, the engineering
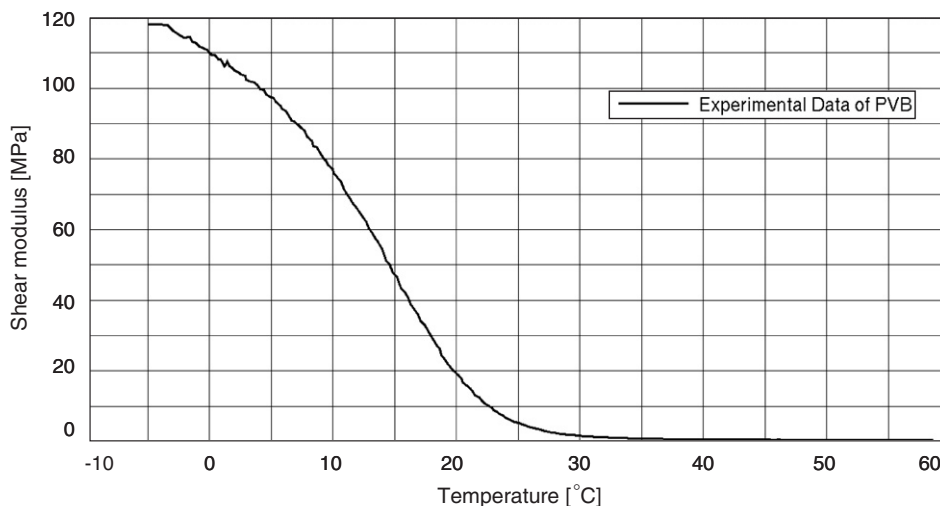


Fig. 1. Shear modulus of PVB for different temperatures.

stress may vary dramatically from the true stress at high strains. This underlines the importance of being careful with experimental data in numerical simulations.

## 2.2. Review of hyperelasticity

Using hyperelasticity, the material behaviour of PVB can be described approximately. For elastic materials, a unique relationship exists between current deformation and stress. The material is called hyperelastic if the stress can be derived from an energy function $W$ that is uniquely related to the current state of deformation. The strain energy depends solely on the deformation gradient $\mathbf{F} = \text{Grad } \mathbf{x}$, whereby this quantity will be symmetrized via the right Cauchy Green strain $\mathbf{C} = \mathbf{F}^{\mathrm{T}}\mathbf{F}$. In the case of an isotropic material the strain energy then depends on the invariants of $\mathbf{C}$ only: $I_C = \mathbf{1} : \mathbf{C} = \text{tr } \mathbf{C}$, $II_C = \frac{1}{2}(I_C^2 - \mathbf{C} : \mathbf{C})$ and $III_C = \det \mathbf{C}$, i.e. $W = \hat{W}(I_C, II_C, III_C)$. The Cauchy stress can now be obtained by $\sigma = J^{-1}\mathbf{F}\mathbf{S}\mathbf{F}^{\mathrm{T}}$, where

$$\mathbf{S} = 2\frac{\partial W}{\partial I_C}\mathbf{1} + 2\frac{\partial W}{\partial II_C}(I_C\mathbf{1} - \mathbf{C}) + 2\frac{\partial W}{\partial III_C}III_C\mathbf{C}^{-1} \tag{1}$$

and $J = \det \mathbf{F}$. Alternatively, the strain energy can be given in dependence of the principal values of $\mathbf{C}$, i.e. $W = \hat{W}(\lambda_1, \lambda_2, \lambda_3)$. The Cauchy stress and Kirchhoff stress in principal directions can be obtained by

$$\sigma_i = \frac{1}{\lambda_j\lambda_k}\frac{\partial W}{\partial \lambda_i} \Rightarrow \lambda_j\lambda_k\sigma_i =: \tau_i = \frac{\partial W}{\partial \lambda_i}. \tag{2}$$

To get the parameters of energy functions with a minimum of effort, simple experiments as uni- or biaxial experiments are widely used. In this case, the eigenvectors $N_i$ of $\mathbf{C}$ are identical to the loading directions, chosen along the global axes and the deformation gradient can be formulated very easily by

$$\mathbf{F} = \begin{pmatrix} \lambda_1 & 0 & 0 \\ 0 & \lambda_2 & 0 \\ 0 & 0 & \lambda_3 \end{pmatrix} \Rightarrow \mathbf{C} = \mathbf{F}^{\mathrm{T}}\mathbf{F} = \begin{pmatrix} \lambda_1^2 & 0 & 0 \\ 0 & \lambda_2^2 & 0 \\ 0 & 0 & \lambda_3^2 \end{pmatrix}. \tag{3}$$

## 3. Numerical treatment

Because of the failure behaviour of the composite, the laminated glass was modelled as follows: If the glass does not fail, the composite acts as a shell, i.e. it is able to transmit normal forces and bending moments. If the glass fails, only the interlayer is able to carry loads, i.e. it acts as a membrane. In our model we realise this behaviour by using two coincident elements: a Belytschko-Tsay shell element for the glass material and a membrane element for the interlayer, see [8,9]. Both types of elements are fully integrated in our simulations so that no hourglass modes should be expected. The glass is modelled as a linear elastic material. If the principle strain reaches a critical value, the glass fails. The use of one shell for the two layers of glass is equivalent to the assumption that both layers fail at the same time. The PVB-interlayer is modelled as a hyperelastic material at first. In Section 3.4 an alternative formulation is presented for the modelling of the interlayer.

## 3.1. Explicit finite element method

In our simulations, we use the explicit solver of LS-DYNA [6]. In this finite element code, Newton's equation of motion

$$M_{ij}\ddot{x}_j(t) + C_{ij}\dot{x}_j(t) + f_i(t) = p_i(t) \tag{4}$$

is solved via a central difference method. The matrices $M_{ij}$ and $C_{ij}$ stand for mass and damping. $f_i(t)$ is the internal nodal resistance in dependence from constitutive law as well as the actually displacement $x_j(t)$ and $p_i(t)$ is the external nodal force. For each time step we have:

$$\dot{x}^n = \frac{1}{2\Delta t}(x^{n+1} - x^{n-1}), \tag{5}$$

$$\ddot{x}^n = \frac{1}{\Delta t}\left(\dot{x}^{n+\frac{1}{2}} - \dot{x}^{n-\frac{1}{2}}\right) = \frac{1}{\Delta t}\left(\frac{x^{n+1} - x^n}{\Delta t} - \frac{x^n - x^{n-1}}{\Delta t}\right)$$
$$= \frac{1}{(\Delta t)^2}(x^{n+1} - 2x^n + x^{n-1}). \tag{6}$$

Inserting Eqs. (6) and (5) in (4) at time $t_n$ yields

$$M_{ij}\left(x_j^{n+1} - 2x_j^n + x_j^{n-1}\right) + \frac{\Delta t}{2}\,C_{ij}\left(x_j^{n+1} - x_j^{n-1}\right) = (\Delta t)^2\left(f_i^n - p_i^n\right). \tag{7}$$

This can be rewritten with respect to the displacement $x^{n+1}$:

$$\underbrace{\left(\frac{1}{(\Delta t)^2}\,M_{ij} + \frac{1}{2\Delta t}\,C_{ij}\right)}_{\hat{M}_{ij}}x_j^{n+1} = \underbrace{p_i^n - f_i^n + \frac{2}{\Delta t^2}\,M_{ij}x_j^n - \left(\frac{1}{(\Delta t)^2}\,M_{ij} - \frac{1}{2\Delta t}\,C_{ij}\right)x_j^{n-1}}_{\hat{p}_j^n}, \tag{8}$$

and solved after inverting $\hat{M}_{ij}$ :

$$x_i^{n+1} = \hat{M}_{ij}^{-1}\,\hat{p}_j^n. \tag{9}$$

The efficiency of the explicit solver will be increased by using lumped mass matrices $M_{jj}$ and modal damping $C_{jj} = \alpha M_{jj}$. Thus, solution of Eq. (9) is trivial.

## 3.2. Incompressibility

The PVB-interlayer is nearly incompressible, i.e. Poisson's ratio is $v \approx 0.5$. For small deformations, this leads to a very large bulk modulus $K$. A standard solution in implicit finite element programs is to minimise the total potential with $J - 1 = 0$ as a side condition using penalty or Lagrange parameter. Note that $J = 1$ corresponds to a divergence free displacement field for small deformation: div $\mathbf{u} = 0$. Alternatively, a mixed formulation (e.g. Q1P0) with different formulation for pressure and displacements is also possible. In an explicit finite element code, we augment the strain energy density $W$ by a penalty function $f(J)$, e.g. $f(J) = \frac{1}{2}K(J - 1)^2$, $f(J) = K \ln J$ and $f(J) = K(J - 1 - \ln J)$. For any deviation from $J = 1$, the function $f(J)$ is penalised by a large bulk modulus $K$.

## 3.3. Material laws

In what follows, we give an overview of hyperelastic material laws, which are widely used in crash simulations. For a general aspect of material modelling with laws implemented in LS-DYNA, see [10]. Note that all material parameters are functions of the strain rate and the temperature, respectively.

### 3.3.1. Blatz–Ko material
The Blatz–Ko energy function [11] is given in a general form by

$$W = \frac{\mu}{2}\left[I_C + \frac{1}{\alpha}\left(III_C^{-\alpha} - 1\right) - 3\right] + \frac{\mu}{2}(1 - \beta)\left[\frac{II_C}{III_C} + \frac{1}{\alpha}\left(III_C^{\alpha} - 1\right) - 3\right], \tag{10}$$

where $\alpha = -(1 - 2v)^{-1}$. In LS-DYNA, the Blatz–Ko material is implemented for $\beta = 1$ which yields

$$W = \frac{\mu}{2}\left[I_C - 3 + \frac{1}{\alpha}\left(III_C^{-\alpha} - 1\right)\right]. \tag{11}$$

Using Eq. (1), the derivative of Eq. (11) results in

$$\mathbf{S} = \mu\left(\mathbf{1} - 2J^{-2\alpha-1}\frac{1}{2}J\mathbf{C}^{-1}\right) \Rightarrow \sigma = \frac{\mu}{J}(\mathbf{FF}^{\mathrm{T}} - J^{-2\alpha-1}\mathbf{1}), \quad -2\alpha - 1 = -\frac{1}{1-2v}. \tag{12}$$

### 3.3.2. Mooney–Rivlin material

A standard function to describe rubber-like behaviour is the material law given by Mooney and Rivlin [12,13]:

$$W(I_C, II_C, III_C) = A(I_C - 3) + B(II_C - 3) + C\left(\frac{1}{III_C^2} - 1\right) + D(III_C - 1)^2. \tag{13}$$

here, $A$ and $B$ are material parameters. The last two expressions with the parameters $C$ and $D$ are hydrostatic terms:

$$C = \frac{A}{2} + B \quad \text{and} \quad D = \frac{A(5v-2) + B(11v-5)}{(2-4v)}. \tag{14}$$

This allows a numerical treatment without constraints. The small strain shear modulus correlates to $\mu = 2(A + B)$ and the Piola-Kirchhoff stress is given by

$$\mathbf{S} = 2(A + BI_C)\mathbf{1} - 2B\mathbf{C} + 4(DJ^2(J^2 - 1) - CJ^{-4})\mathbf{C}^{-1}. \tag{15}$$

A stress-free state requires $(14)_1$ directly. For uniaxial tension or compression, the deformation gradient is given by

$$\mathbf{F} = \begin{pmatrix} \lambda & 0 & 0 \\ 0 & \lambda^{-1/2} & 0 \\ 0 & 0 & \lambda^{-1/2} \end{pmatrix} \Rightarrow \frac{\tau}{2\left(\lambda - \frac{1}{\lambda^2}\right)} = A + \frac{B}{\lambda}. \tag{16}$$

This allows to determine $A$ and $B$ by fitting experimental data: first transform the engineering stress and strain:

$$\tau \mapsto \frac{\tau}{2\left(\lambda - \frac{1}{\lambda^2}\right)}, \quad \varepsilon \mapsto \frac{1}{1+\varepsilon} = \frac{1}{\lambda}. \tag{17}$$

Then, the gradient of a linear fit obtained by this curve gives the material parameter $B$ and the intersection with the ordinate gives $A$.

### 3.3.3. Ogden material

The material laws (11) and (13) are special cases of a more general function derived by Ogden, see [14,15]:

$$W = \sum_{i=1}^{3}\sum_{j=1}^{n}\frac{\mu_j}{\alpha_j}\left(\lambda_i^{*\alpha_j} - 1\right) + K(J - 1 - \ln J). \tag{18}$$

Here, $\alpha_j$ are non-integer, $J = \lambda_1\lambda_2\lambda_3$ and $\lambda_i^* = \lambda_i J^{-1/3}$. Using $\partial J/\partial \lambda_i = \lambda_j\lambda_k$, the derivative of Eq. (9) yields

$$\frac{\partial W}{\partial \lambda_i} = \tau_i = \sum_{j=1}^{n}\mu_j\left[\frac{\lambda_i^{*\alpha_j}}{\lambda_i} - \frac{1}{3}\frac{\lambda_i^{*\alpha_j}}{\lambda_i} - \frac{1}{3}\frac{\lambda_j^{*\alpha_j}}{\lambda_i} - \frac{1}{3}\frac{\lambda_k^{*\alpha_j}}{\lambda_i}\right] + \frac{K(J-1)}{J}\lambda_j\lambda_k \tag{19}$$

from which we can calculate the Cauchy stress

$$\sigma_i = \sum_{j=1}^{n}\frac{\mu_j}{J}\left[\lambda_i^{*\alpha_j} - \sum_{k=1}^{3}\frac{\lambda_k^{*\alpha_j}}{3}\right] + \frac{K(J-1)}{J}. \tag{20}$$

Clearly, the first terms are purely deviatoric and the pressure is entirely contained in the penalty term based on a relatively high bulk modulus $K$. In the incompressible case, we have $J = 1$ and $\lambda_i^* = \lambda_i$. The
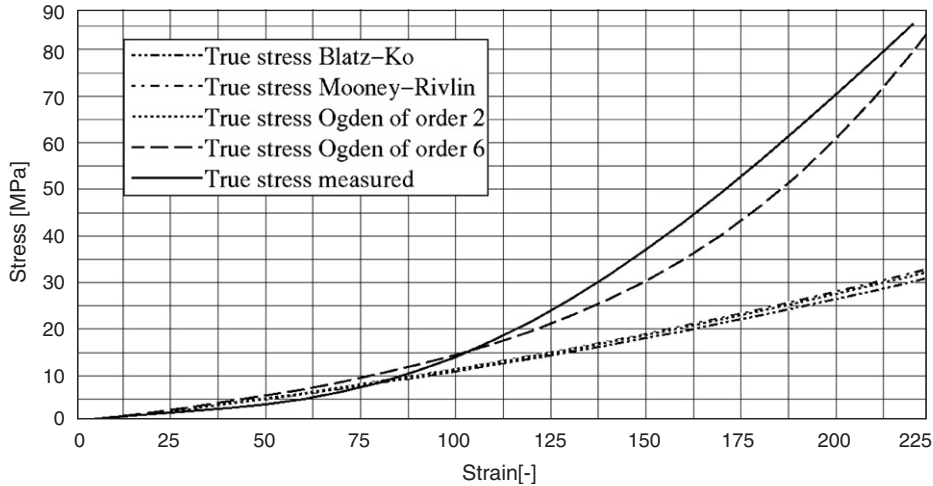
Fig. 2. Validity tests for the material modelling of PVB.

Mooney–Rivlin law is obtained for $n = 2$, $\alpha_1 = 2$, $\alpha_2 = -2$, $\mu_1 = 2A$ and $\mu_2 = -2B$; e.g. the deviatoric part is given by

$$
\begin{aligned}
W &= \frac{\mu_1}{2}\left(\lambda_1^2 + \lambda_2^2 + \lambda_3^2 - 3\right) + \frac{\mu_2}{-2}\left(\lambda_1^{-2} + \lambda_2^{-2} + \lambda_3^{-2} - 3\right) \\
&= \frac{\mu_1}{2}(I_C - 3) + \frac{\mu_2}{-2}\left(\lambda_1^2\lambda_2^2 + \lambda_2^2\lambda_3^2 + \lambda_3^2\lambda_1^2 - 3\right) \\
&= \frac{\mu_1}{2}(I_C - 3) + \frac{\mu_2}{-2}(II_C - 3).
\end{aligned}
\tag{21}
$$

Fig. 2 shows the best fit for the different materials laws in comparison to the experimental data taken from D'Haene [5]. For small deformations, the Blatz–Ko and the Mooney–Rivlin material (we chose $A = 1.60\,\text{MPa}$ and $B = 0.06\,\text{MPa}$) are in a good agreement with the PVB data. For large deformation, it is necessary to consider higher order terms in the Ogden law. An Ogden material of order six (dashed line) leads to a curve that is close to the experiment (solid line).

### 3.4. A smeared modelling technique

For some applications it is important to compute the acceleration of an impactor for certification, e.g. in pendulum impact test [20]. For a bending load, however, the suggested model is not suitable because the interlayer is not able to simulate the ultimate load bearing capacity with respect to the condition after fracture. The suggested model represents all parts of the windscreen without considering any composite efficiency. Therefore, a smeared modelling technique is introduced by using two coincident shell elements with the same thickness. Hence, the stiffness before fracture has to be adjusted by considering an equivalent thickness $t_E$ of the shells and the density of the elements has to be readjusted to maintain the correct, total mass. The membrane is modelled by bilinear plasticity now, smearing the behaviour of interlayer and glass fragments, see [18,19]. Because of the dynamic loading, full bonding between glass and interlayer may be assumed. Considering laminated glass with Young's moduli $E_G$, $E_{PVB}$, a total thickness of $t = 2t_G + t_{PVB}$, and the densities $\rho_G$, $\rho_{PVB}$, the required equivalent thickness

$$
t_E = \sqrt[3]{t_G^3 + 3t_G(t_G + t_{PVB})^2 + \frac{E_{PVB}}{2E_G}\,t_{PVB}^3}
\tag{22}
$$

of the coincident shells is obtained. The modified density then becomes

$$
\rho_E = \left(\rho_G t_G + \tfrac{1}{2}\rho_{PVB} t_{PVB}\right)/t_E.
\tag{23}
$$

The bending stiffness of the two coincident shell elements with the equivalent thickness $t_E$ and the modulus of glass $t_G$ is identical to the bending stiffness of the 3-layered laminated glass composite. A further refinement must now be added to the model in order to allow the modelling of glass failure.

We assume that the glass layer on the tensile side of the windscreen looses all stiffness after failure whereas the glass layer on the compressive side remains intact. The centre of gravity is then relocated according to parallel axis theorem. At failure, one of the two shell elements in the model is eroded, this allows to compute the Young's modulus for the state after fracture of the remaining shell element as follows:

$$E^{II} = \frac{1}{t_E^3} \left[ E_G \left( t_G^3 + 3 t_G t_{PVB}^2 \right) + E_{PVB} \left( t_{PVB}^3 + 3 t_{PVB} t_G^2 \right) \right]. \tag{24}$$

Consequently one shell element in the model with a Young's modulus given as $E_{PVB,mod} = E^{II}$ will never erode and can be considered to represent the interlayer and the compressive side of the glass in the windscreen. The second shell element is given by a Young's modulus $E_{G,mod} = 2E_G - E^{II}$ in order to maintain the correct bending stiffness before failure. This equivalent glass element exhibits brittle rupture as before. A bilinear elasto-plastic material law is used to represent the non-linear aspect of the material behaviour whereby the yield stress and the tangent modulus may be used to validate the model with respect to experimental results. Since the entire approach is based upon the use of classical material laws, all necessary options for this methodology are available in commercial FE-codes and no specific development has been performed.

## 4. Applications

### 4.1. Four-point bending test

First of all, we try to simulate a four-point bending test for the validation of our model in comparison with experimental results. The experimental set-up consists of a laminated glass plate (length = 1100 mm, width = 600 mm, total thickness = 6.72 mm, 0.72 mm PVB) bearing-supported by two cylinders (diameter = 50 mm, distance = 1000 mm). The plate is loaded by two cylinders (diameter = 50 mm, distance = 200 mm) for which we increase the displacement slowly (quasi-static) up to 30 mm, see Figs. 3 and 4. At first, the laminated glass model corresponds to the original approach, For the glass we used a Young modulus of $E = 70$ GPa, a Poisson ratio of 0.23 and a failure-strain of 0.15%. The Blatz–Ko law was used for the PVB interlayer.
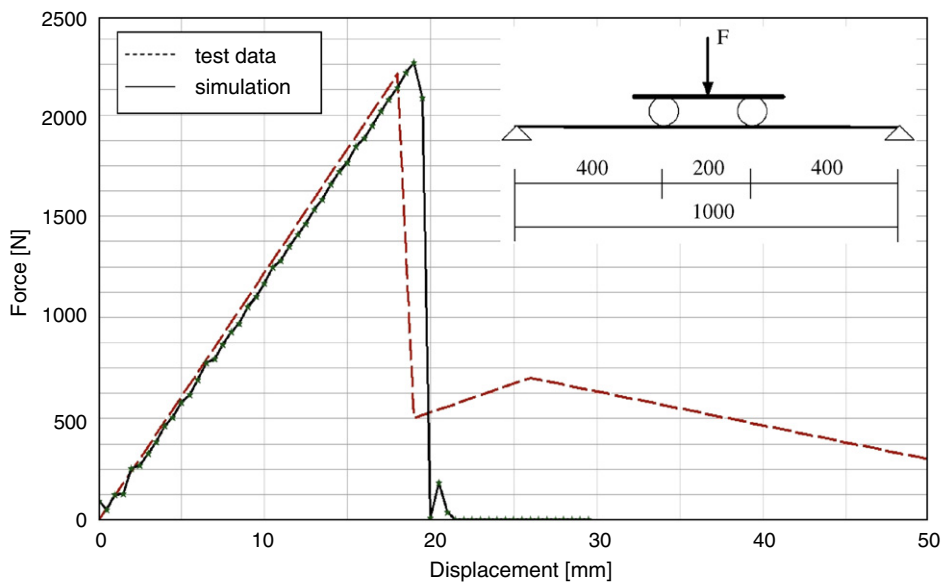


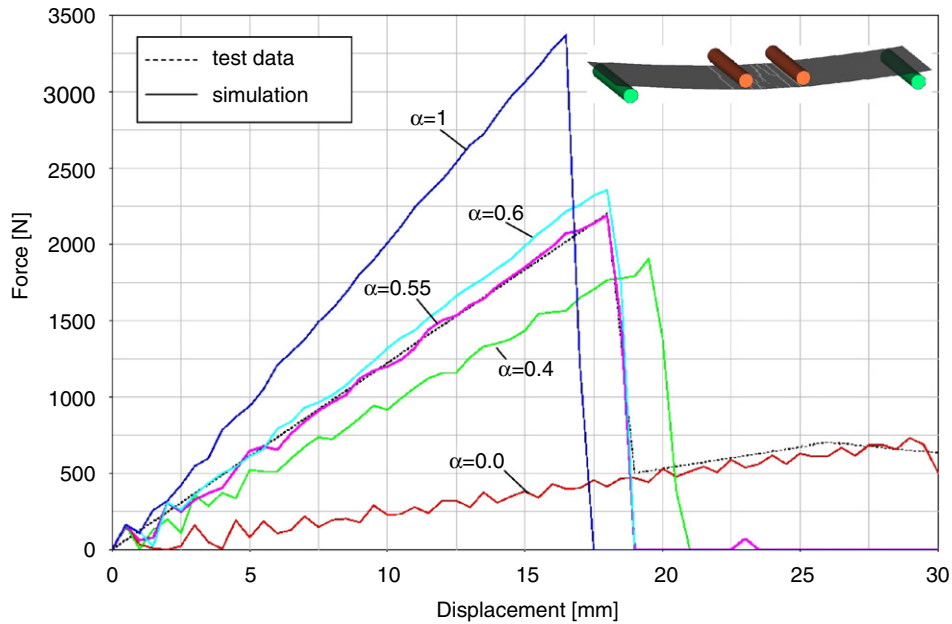Fig. 3. Validation test for the laminated glass model.

Fig. 4. Validation test for the modified laminated glass model.

In Fig. 3, the reaction force is plotted versus the prescribed displacement of the cylinder. As can be seen, the numerical and the experimental results are in a good agreement. However, a quasi-static solution is hard to achieve using explicit finite element method. After a displacement of 20 mm, the glass fails and there is no contact left between the cylinders and the PVB. Therefore, the load carrying capacity of the PVB could not be checked by this test.

In Fig. 4, the same test has been simulated with the smeared formulation. However, the assumption of full bonding between glass and interlayer is valid for dynamic loading only. This is due to creep behaviour of the PVB interlayer, which depends on temperature and time. Consequently, the composite efficiency is considered by an additional factor $\alpha$ in the parallel axis theorem according to $I = \sum I_i + \alpha z_{si} A_i$, where $\alpha = 0$ if no bonding exists and $\alpha = 1$ in the case of full bonding, where both panes behave like a single one. With this formulation and from Eqs. (22)–(24), values for the element thickness, the density and the Young's modulus of the two shells can be determined. In this example, the factor $\alpha$ has been varied to find the composite efficiency of the laminated glass in this quasistatic example. It can be seen that a good correlation with the test result is obtained for $\alpha = 0.55$ which yields for the individual layer properties: $t_E = 8.74$ mm, $\rho_E = 1.72$ kg/dm$^3$, $E_{PVB,mod} = 23220$ MPa and $E_{G,mod} = 116780$ MPa. In the subsequent dynamic examples, $\alpha = 1$ is assumed and thus $t_E = 10.13$ mm, $\rho_E = 1.48$ kg/dm$^3$, $E_{PVB,mod} = 15260$ MPa and $E_{G,mod} = 124740$ MPa.

### 4.2. Robustness study: impact of a rigid sphere

As a purely numerical example, we simulate the impact of a rigid sphere with a laminated glass plate. Purpose of this study is to demonstrate the numerical robustness of the model for which no experimental work is required. The plate is chosen to be quadratic (length = 1500 mm, thickness = 5.00 mm for the shell and 0.38 mm for the membrane) and all degrees of freedom at the boundaries are fixed. A regular arrangement of $60 \times 60$ elements is used for discretization. We assume a failure-strain of 0.1% for the glass (reduction of the static value because of dynamic loading) and no failure for the interlayer. For the sphere, we chose a diameter of 300 mm, a mass of 70 kg and an initial velocity of 10 m/s.

Fig. 5 shows the temporal evolution of the impact. At 10 ms, the first elements fail and cracks start to propagate in different directions. The bright areas are failed elements where only the PVB-interlayer carries the load. Between 30 and 40 ms, some larger glass fragments are formed, which are still joined by the
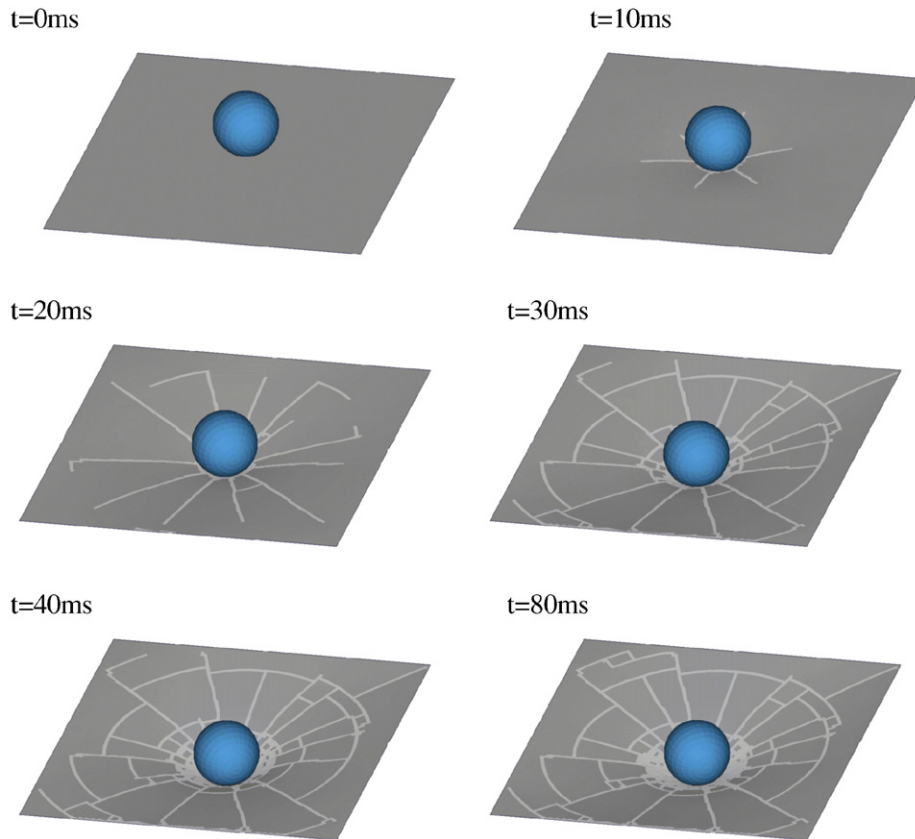
Fig. 5. Temporal evolution of the impact (irregular meshing).

membrane. This can be observed till the end of the impact at 80 ms. The simulation shows a quite realistic fracture pattern of the laminated glass. This fracture pattern is very sensitive to mesh refinement and orientation. However, the displacement of the plate during the impact is not very mesh dependent. This will be shown in the following.

The discretization of the structure using a regular rectangular grid based on quadrilateral elements does not always allow for a correct prediction of the crack pattern. Hence, alternative mesh topologies were used and the qualitative and quantitative influence of the mesh on different results was investigated. This procedure is possible for the present example because we consider only a single load condition to which we could adapt the mesh. A hybrid mesh consisting of triangular and quadrilateral elements was developed, allowing a pattern of radial and tangential meshlines. Additionally, we used a mesh consisting solely of triangular elements. Fig. 6 shows the different fracture patterns that were obtained using different mesh topologies. The upper part of Fig. 6 shows the fracture pattern obtained with the hybrid, radial-tangential mesh. This corresponds closely to the observed behaviour in the test and shows a clear improvement versus the results obtained with the rectangular grid shown in the lower part of Fig. 6. In the middle part of this picture, we show the fracture pattern obtained by the mesh based uniquely on triangular elements. This mesh clearly results in a non-realistic fracture pattern. In the perspective views in Fig. 5 for different sequences of the impact simulation using the radial-tangential grid, the effect of the mesh topology on the crack pattern is visible.

It might be more interesting to consider the qualitative effects of the mesh type on the displacement or intrusion values of the impactor for instance. Therefore, we plotted the displacement-time curves that were obtained for different discretizations in Fig. 7. The curves show only a negligible dependency of the intrusion values upon the mesh topology and a clearer influence of the mesh size. Indeed, the difference in intrusion obtained by quadrilateral and triangular elements of comparable sizes is not significant. The same is true if we compare quadrilateral elements of the same size in rectangular versus radial grids. However, what can be

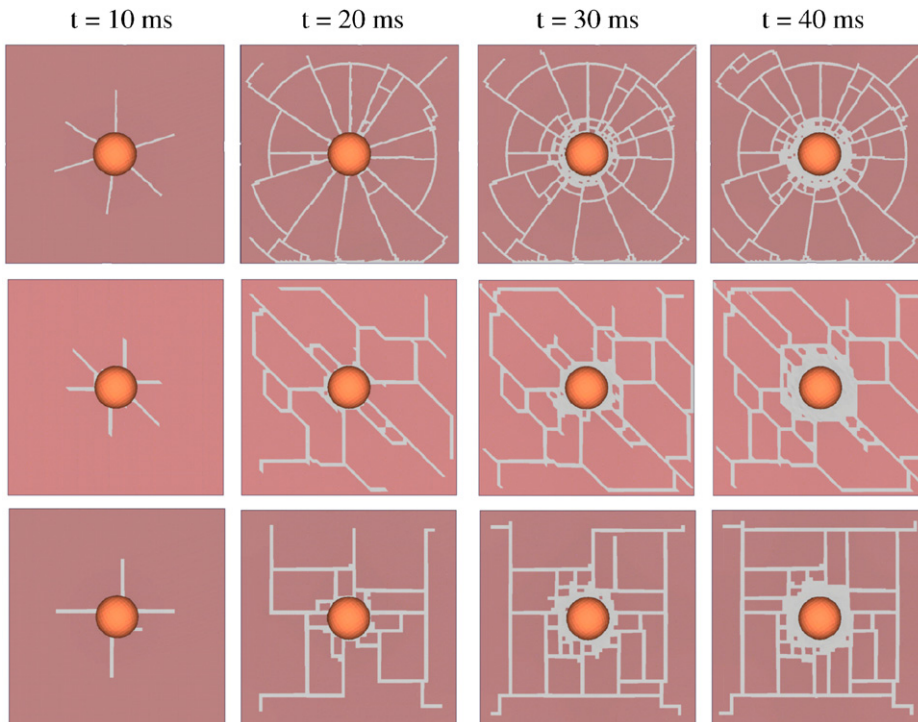t = 10 ms        t = 20 ms        t = 30 ms        t = 40 ms



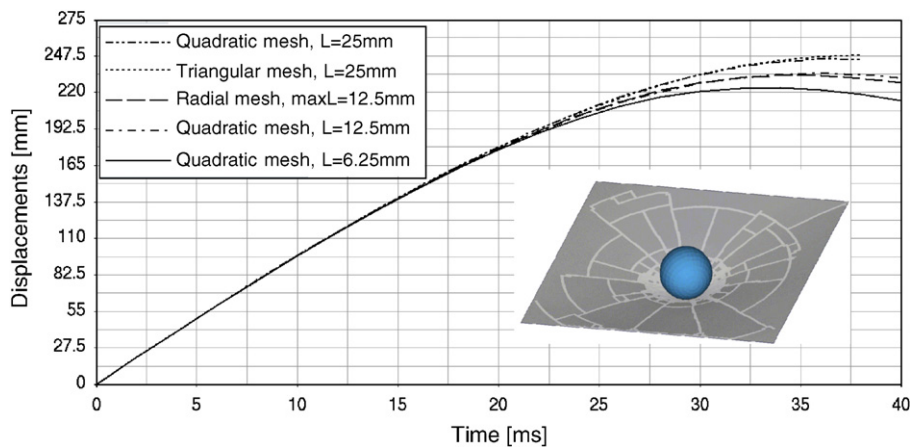Fig. 6. Mesh dependency of the fracture behaviour.



Fig. 7. Mesh dependency of the displacements.

observed is a decrease of the intrusion values if the mesh is progressively refined. This seems to be independent of the mesh topology and could be related to an exaggerated effect of element elimination in coarse meshes. The smeared model leads to comparable results.

## 4.3. Roof crush

As a practical example, we investigate a windshield during a roof crush of a vehicle. In the numerical simulation, the impactor is modelled as a rigid wall which loads the structure with an initial velocity of 2 m/s. The lower side of the structure is fixed in vertical direction ($z$), the A-pillar is fixed in $x$- and $y$-direction additionally.

Simulations of the roof crush test were performed using both the hyperelastic and the smeared models for the PVB interlayer. The chronological evolution of the roof crush is depicted in Fig. 8 for the model using a hyperelastic PVB model: After 40 ms, the first elements fail and at the end of the calculation at 100 ms some larger glass fragments have formed. The fracture pattern and the intrusion of the A-pillar are in a good agreement with real crash tests. In Fig. 9, the (normalised) resulting force acting on the rigid wall is plotted vs. displacement for test (thin line) and simulations (thick lines). For this load case, both models (hyperelastic and
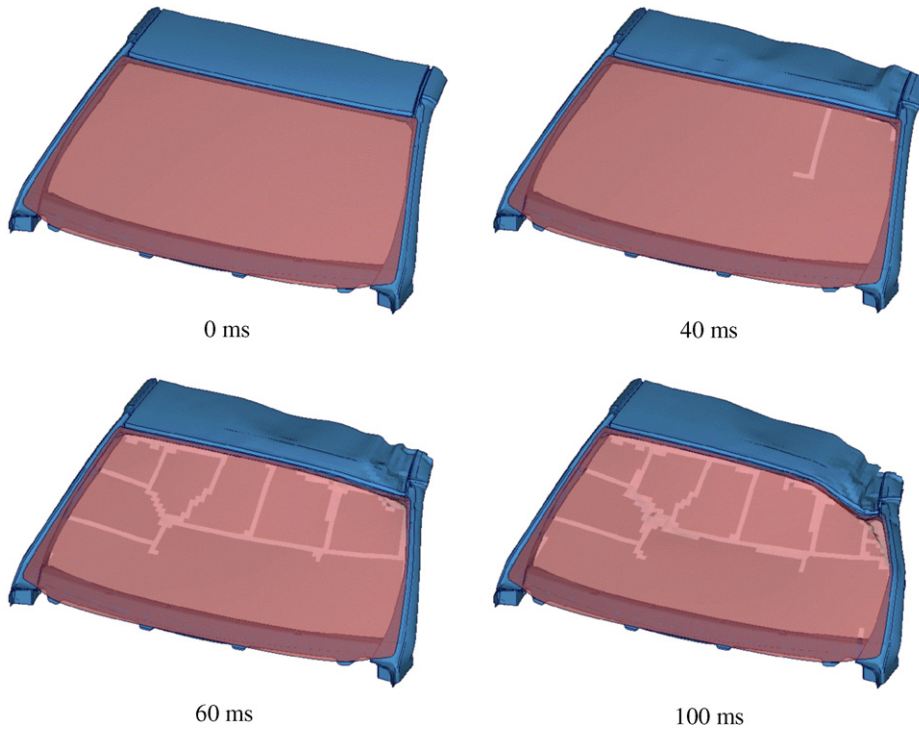


0 ms 40 ms

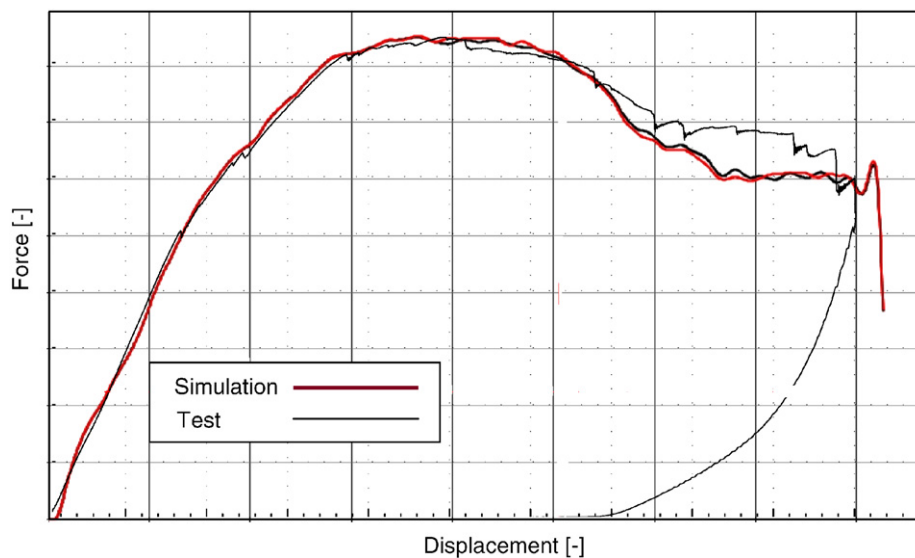60 ms 100 ms

Fig. 8. Windshield during roof crush.



Fig. 9. Force versus displacement during roof crush.

smeared model) predict the test very good. This allows a precise and reliable prediction with respect to the fulfilment of the requirements of laws and standards in the automotive industry.

### 4.4. Validation via impact test

It has been shown in the last example that the hyperelastic model behaves pretty well in the simulation of the kind of loading that occurs during a roof crush. If the load is applied perpendicular to shell plane, though, the material response of this model is too soft. This has been shown in [17] for a pendulum test and the same experience has been gained from the subsequent validation test. Therefore, the hyperelastic model is replaced by the smeared model in the subsequent simulations.

Basis for validation was an experimental investigation following Browne [16] where a sphere-like impactor (outer diameter of 170 mm, mass of 3.5 kg) has been shot with a velocity of 35 km/h on the middle of a windscreen under a prescribed angle of 50° with respect to the horizontal. In total six tests have been carried out and for validation, average values of the acceleration are used. The fracture pattern of the windshields are shown in Fig. 10.
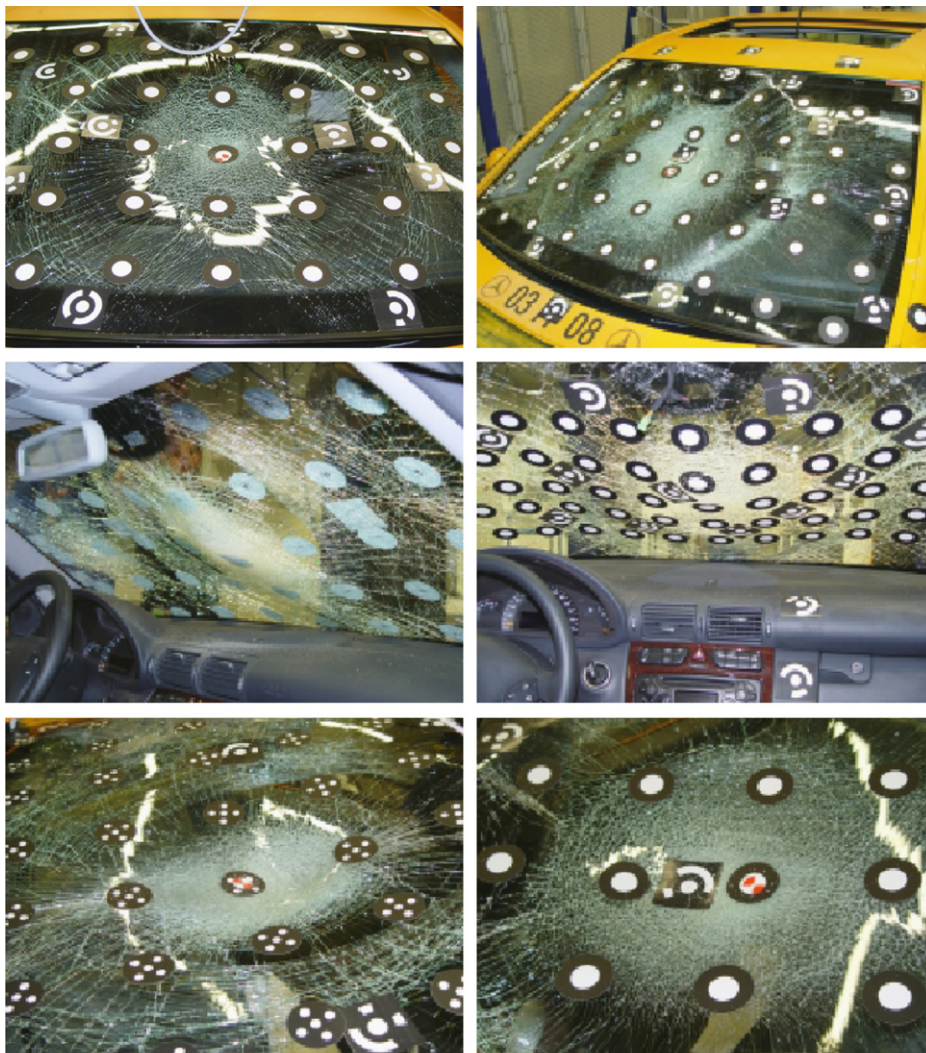


tests 1 to 3                                 tests 4 to 6

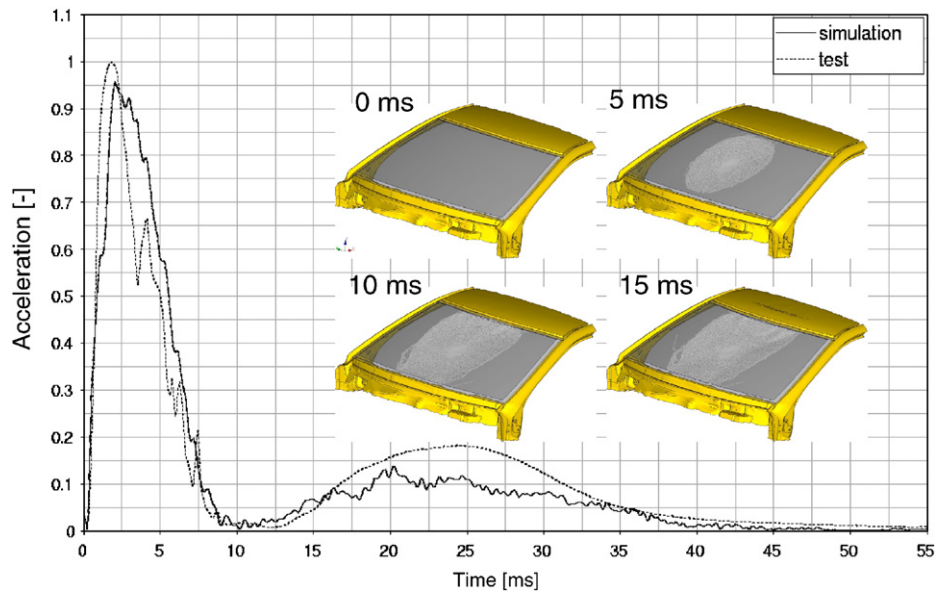Fig. 10. Fracture patterns of the windshields.

Fig. 11. Comparison of the simulation with test results.

In Fig. 11, the normalised acceleration of the impactor is plotted vs. time. Within 2 ms, maximum acceleration is developed in the impactor. After this point, the glass fails extensively in the impacted region. Subsequently, the shape of the curve is strongly influenced by the fracture behaviour of the windshield. This results in large scatter of both experimental and numerical results. The period of the impact is roughly 10 ms. Ensuing acceleration is based on the elastic rebound of the windshield. The chronological evolution of the fracture pattern during the impact is likewise depicted in Fig. 11. It should be emphasized, however, that a lot of unknown parameters exist in such a rather complex model, e.g. influence of adhesives and other structural parts among others. The identification of these parameters may be very difficult.

## 5. Conclusions and outlook

Laminated glass models are suggested consisting of two coincident finite elements. In a first approach a shell element for the glass and a membrane element for the interlayer have been used. The model considers both the failure of the glass and the hyperelastic behaviour of the PVB-interlayer. For strains less than 100%, a Blatz–Ko material and a Mooney–Rivlin material are suitable to model PVB. In general, an Ogden material of order six is recommended. This numerically robust model is capable of simulating qualitatively realistic fracture behaviour of laminated glass and leads to good agreements with experimental findings in a roof crush simulation. Though for impact simulations, the model is not suitable to describe the bending stiffness appropriately. Therefore, a modified approach using a smeared formulation of glass and interlayer is suggested. With this modification, the acceleration of an impactor shot on a windscreen could be simulated in a satisfactory way. Furthermore, the model can be used to identify the composite efficiency of laminated glass in a simple four-point bending test.

As for the modelling technique, further investigations are desirable to avoid the coincident element formulation, e.g. by assigning the different material properties to the Gauss points directly. In addition, the assumption to neglect the viscous effects in both models is unsatisfactory and has to be reconsidered in the future.

## References

[1] Chlastawa S, Horaney S. Evaluating the intrusion resistance of installed motor vehicle glazing. Society of Automotive Engineers, Inc.; 1997 98IBECG-15.

 [2] Kolling S, Fassnacht W, Du Bois PA. Numerical simulation of a windshield for crashworthiness. Germany: LS-DYNA Forum, Bad Mergentheim; 2002 V33:1–10.
 [3] Du Bois PA, Kolling S, Fassnacht W. Modelling of safety glass for crash simulation. Comput Mater Sci 2003;28(3–4):675–83.
 [4] Kordisch H, Varfolomeev I, Sester M, Werner H. Numerical simulation of the failure behaviour of wind-shields. Vienna, Austrian: 32nd ISATA; 1999. pp. 299–306.
 [5] D'Haene P. Experimental data of PVB. Belgium: Solutia Europe SA/NV; 2002.
 [6] LS-DYNA user manual, Livermore Software Technology Corporation.
 [7] Du Bois PA. Crashworthiness engineering course notes. Livermore Software Technology Corporation; 2004.
 [8] Belytschko T, Tsai CS. Explicit algorithms for nonlinear dynamics of shells. ASME 1981;AMD-48:203–31.
 [9] Belytschko T, Lin J, Tsai CS. Explicit algorithms for nonlinear dynamics of shells. Comp Meth Appl Mech Eng 1984;42:225–51.
[10] Du Bois PA, Fassnacht W, Kolling S. Material modeling with LS-DYNA for crashworthiness analysis. Germany: LS-DYNA Forum, Bad Mergentheim; 2002 V2:1–55.
[11] Blatz PJ, Ko WL. Application of finite elastic theory to the deformation of rubbery materials. Trans Soc Rheol 1962;6:223–51.
[12] Mooney M. A theory of large elastic deformations. J Appl Physics 1940;11:582–92.
[13] Rivlin RS. Large elastic deformations of isotropic materials. Proc Roy Soc London 1948;241:379–97.
[14] Ogden RW. Large deformation isotropic elasticity: on the correlation of theory and experiment for incompressible rubberlike solids. Proc Roy Soc London 1972;326:565–84.
[15] Ogden RW. Elastic deformations of rubberlike solids. In: Hopkins HG, Sewell MJ, editors. Mechanics of solids, The Rodney Hill 60th anniversary volume. Oxford: Pergamon Press; 1982. p. 499–537.
[16] Browne AL. 2-Ply Windshields: Laboratory Impactor Tests of the Polyvinyl Butyral/Polyester Construction. SAE-Paper No 950047, 1995.
[17] Nguyen NB, Haufe A, Sonntag B, Kolling S. On the impact simulation of safety glass. Part I: Finite element models for tempered and laminated safety glass. Proceedings of the third LS-DYNA forum, Bamberg, Germany, C-I-13/24, 2004.
[18] Haufe A, Nguyen NB, Sonntag B, Kolling S, On the impact simulation of safety glass. Part II: Validation of a finite element model for laminated safety glass. Proceedings of the third LS-DYNA Forum, Bamberg, Germany, C-I-25/36, 2004.
[19] Schneider F, Sonntag B, Kolling S. Numerical and experimental investigation of the behaviour of laminated safety glass with respect to the condition after fracture. Bauingenieur 2004;79:516–21.
[20] Brendler S, Haufe A, Ummenhofer T. A detailed numerical investigation of insulated glass subjected to the standard pendulum test. Proceedings of the third LS-DYNA Forum, Bamberg, Germany, F-I-57/64, 2004.